Laser Powder Bed Fusion of ODS Fe–Cr–Al (0.3Zr, 0.3Y_2O_3): Unveiling Processing-Microstructure- Mechanical Property Relationships

Subhashish Meher[1], Chinthaka M. Silva[1], Holden Hyer[2], Tanvi A. Ajantiwalay[1], Shalini Tripathi[1], Angel Ortiz[1], Quin R. S. Miller[1], Nathan Canfield[1], Mohan Sai Kiran Kumar Yadav Nartu[1], Sebastien Dryepondt[2], Isabella J. van Rooyen[1]

[1]Pacific Northwest National Laboratory, Richland, WA 99354, USA
[2]Oak Ridge National Laboratory, TN 37831, USA
Correspondence: Subhashish.Meher@pnnl.gov

Abstract:

This study employs laser powder bed fusion (LPBF) additive manufacturing for the fabrication of a novel oxide dispersion strengthened (ODS) Fe-Cr-Al alloy, designed with strategic additions of 0.3 wt.% Zr and 0.3 wt.% Y_2O_3 to promote oxide dispersion and enhance mechanical robustness. Through a carefully designed experimental matrix, diverse LPBF printing conditions were explored, yielding a spectrum of microstructural outcomes, including one low-density product and two exhibiting near-full density. Characterization confirmed oxide precipitates and minor carbides within the LPBF material, but precipitate density was low (~10^7 cm^{-3}), yielding a sink strength of ~10^7 m^{-2}. Microhardness values were typical for FeCrAl alloys (mid-200s HV). Notably, microhardness correlated indirectly with average grain size, adhering to the Hall-Petch relationship, rather than directly with oxide distribution. These findings offer critical insights into the challenges and opportunities associated with LPBF fabrication of ODS Fe-Cr-Al alloys. Meticulous control over LPBF processing parameters and post-processing treatments are paramount to tailor precipitate nucleation, growth, and distribution, thus governing the alloy's final mechanical performance.

Keywords: Additive Manufacturing; ODS steels; Laser Powder Bed Fusion, FeCrAl

1. Introduction

Advanced nuclear energy systems, including Generation IV reactors and concept for Accident Tolerant Fuels (ATF), demand structural components that can withstand unprecedented operational demands. The materials employed in these reactors must endure extreme conditions, including high temperatures exceeding current light water reactors (LWR) designs, highly corrosive coolants such as molten salts and supercritical fluids, and intense neutron irradiation fluxes leading to high atomic displacement damage (dpa). These coupled stressors necessitate materials with exceptional long-term stability, resistance to irradiation-induced degradation, and immunity to environmentally assisted failure mechanisms. Conventional ferritic/martensitic and austenitic steels, despite decades of optimization, fundamentally lack the microstructural stability and property retention necessary under such extreme conditions.

Given these nuanced considerations, oxide dispersion strengthened (ODS) Fe-Cr-Al ferritic alloys represent an attractive alternative pathway towards developing high-performance structural materials for advanced reactors [1-6]. Beyond the exceptional mechanical strength afforded by nanoscale dispersoids with density nearly 10^{16} particles/cm^3, the strategic incorporation of aluminum provides multifaceted benefits: it suppresses radiation-induced α' precipitation (particularly at optimized 10-12% Cr levels) [7-12], contributes solid solution strengthening, and facilitates the formation of extraordinarily protective Al_2O_3 surface films [13-15].

These advanced materials—particularly variants containing 9-19% chromium—demonstrate remarkable performance enhancements compared to conventional steel counterparts. The exceptional high-temperature stability and irradiation resistance of ODS alloys derive from nanoscale oxide precipitates (primarily Y_2O_3 and its derivatives such as Y-Al-O, Y-Ti-O, and Y-Al-Ti-O complexes) [1] that effectively pin dislocations, stabilize grain boundaries, and serve as recombination sites for radiation-induced defects.

While 13-14Cr ODS variants (exemplified by the extensively studied 14YWT) [16] exhibit extraordinary mechanical strength and creep resistance at elevated temperatures, significant challenges persist [17] regarding their industrial implementation. These include limited tensile ductility resulting from intrinsic embrittlement mechanisms and radiation-induced fracture susceptibility stemming from α'-phase precipitation in high-Cr compositions (>12% of ferrite-forming elements including Cr, Mo, and Ti). These limitations have accelerated the exploration of alternative ODS compositions with optimized property balances. The exceptional oxidation resistance, coupled with superior high-temperature strength and radiation damage tolerance, positions ODS FeCrAl among the most promising accident-tolerant materials for both advanced fission and fusion energy systems.

The fabrication of ODS alloys with optimized microstructures remains a critical barrier to their widespread implementation. Conventional powder metallurgy routes—involving mechanical alloying, consolidation, and thermomechanical processing—present significant challenges including inconsistent dispersoid distributions, limited geometric complexity, and substantial material waste [18]. Additive manufacturing (AM) technologies offer a revolutionary alternative, potentially enabling un-precedented control over nano/microstructural features while simultaneously facilitating complex component geometries unattainable through traditional manufacturing approaches.

In this study, laser powder bed fusion (LPBF) additive manufacturing is utilized to fabricate ODS FeCrAl with a composition of Fe-10Cr-6.1Al-0.3Zr-0.3Y_2O_3 under varying experimental conditions. This research seeks to establish a fundamental under-standing of the relationship between LPBF processing parameters, microstructure evolution, and the resulting properties of ODS FeCrAl alloys, contributing to the advancement of AM-enabled manufacturing of advanced structural materials for next-generation nuclear energy systems.

2. Materials and Methods

2.1 Materials

Fe-12Cr-6.1Al-0.3Zr (wt.%) powder (gas atomized, ATI Powder Metals) was mechanically alloyed with 0.3 wt.% nanocrystalline yttria (17-31 nm diameter) using a CM08 Simoloyer under Ar. Based on prior work demonstrating optimal yttria dispersion, a 40-hour ball milling process with alternating rotation speeds (350-600 rpm) was employed. [8, 18, 19].

A Renishaw AM250 laser powder bed fusion (LPBF) system, configured with a reduced build volume, was employed to optimize printing parameters for the ODS FeCrAlYZr powder. Small cube samples (5 × 10 mm cross-section) were fabricated to assess the influence of key processing parameters—laser power (P), point distance (PD), dwell time (DT), hatch spacing (HS), and layer thickness (T)—on Archimedes density. While a full description of the optimization process is not within the scope of this paper, the selection of characterized samples was guided by cube density and printing energy density (ED) defined as:

$$ED=P/(PD/(DT+D)\cdot HS\cdot T) \qquad (1)$$

where D is the delay time of the pulsed laser, taken as 10 µs. The quotient of the PD and DT+D can be equated to the raster scan speed for a continuous wave laser.

A total of 12 FeCrAlZr samples were fabricated via LPBF. Cube samples (10 mm^3) were extracted from the builds for density measurements. Fig. 1 illustrates the relationship between cube density and energy density, revealing an increase in density with increasing energy density up to 100 J/mm^3, followed by a plateau at ~7.15 g/cm^3. Based on this density plateau, samples 9 and 12 (designated LPBF CrAZY9 and LPBF CrAZY12, respectively) were selected to represent the lower and upper density bounds. Cube 3 (LPBF CrAZY3) was chosen to assess the influence of low energy density on microstructural features, anticipating a higher defect concentration.

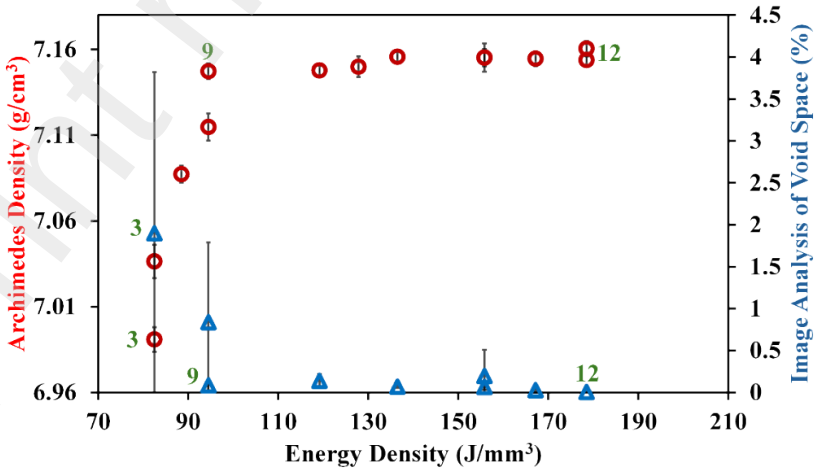

Fig. 1. Density versus energy density plot showing the characterized samples (LPBF CrAZY3 [#3], LPBF CrAZY9 [#9], and LPBF CrAZY12 [#12]) highlighted in green.

Table 1: LPBF parameters used for sample fabrication, and resulting relative densities (based on Archimedes' method, and the total void space measured by image analysis).

Sample	Laser power (W)	Point distance (µm)	Exposure time (µs)	Hatch spacing (µm)	Energy density (J/mm^3)	Density (g/cm^3)	Void space (%)
CrAZY3	275	80	60	100	82.5	6.99	1.89
CrAZY9	315	80	60	100	94.5	7.15	0.08
CrAZY12	315	160	60	100	178.5	7.16	0.01

2.2 Microstructural characterization

The three LPBF-fabricated samples underwent phase analysis via X-ray diffraction and microstructural characterization using a suite of microscopy techniques, including optical microscopy, scanning and transmission electron microscopy (SEM and TEM, respectively). Specific details for each technique are described below.

2.2.1 X-ray diffraction (XRD)

XRD analysis was performed using a Bruker D8 Discover TXS-HE A25 diffractometer with a rotating Cu anode (Kα λ = 1.54060 Å) and Dectris EIGER2 R 500K detector. Samples were aligned using a laser-video system and positioned with a UMC 1516 motorized stage. A point beam was generated using a Montel optic and 1.0 mm collimator, with the source operating at 45 kV and 120 mA and a source-sample distance of 425 mm. Data were collected over a 2θ range of 10–105° (0.02° step size, 0.2 s/step) and integrated using Bruker EVA software. Rietveld refinement was conducted using GSAS software [20] to fit the XRD patterns, enabling the determination of crystallite size and macrostrain in the α-ferrite phase via Williamson-Hall analysis (see [21] for details).

2.2.2 Optical microscopy and image analysis

Select samples were cross-sectioned, mounted in expoxy, and metallographically prepared using SiC grit papers and diamond colloids. A final finish was performed with 0.05 µm colloidal silica with water. A Keyence VHX-6000 optical microscope was used to image the samples. Depending on the cross-section, 6–12 images were imaged at 200× from each sample and processed using a python (version 3.12) script that performs the following analysis: converts images to 8-bit, thresholds to black (solid material) and white (void space) contrast, and a final calculation of the total void space area percentage. The void space percentage is shown in tandem with the Archimedes density in Fig. 1, and specific values for the CrAZY3, CrAZY9, and CrAZY12 are reported in Table 1.

2.2.3 Scanning electron microscopy (SEM) and electron back-scatter diffraction (EBSD)

Polished samples were analyzed using SEM coupled with electron backscatter diffraction (EBSD) and energy dispersive spectroscopy (EDS). SEM/EBSD data were collected using either a FEI Quanta FEG FIB, a Helios Hydra Plasma FIB, or a JEOL 7600 SEM, while elemental compositions were determined using EDS. Both backscatter electron (BSE) and secondary electron (SE) imaging modes were employed. Data acquisition and analysis for EBSD and EDS were performed using AZtecCrystal software (Oxford Instruments)

2.2.4 Transmission electron microscopy (TEM)

Microstructural characterization was further performed using a JEOL Grand Arm Scanning TEM (STEM) operated at 300 keV. Conventional bright-field (BF), high-resolution (HR), and high-angle annular dark-field (HAADF) imaging modes were employed. High-resolution elemental mapping was conducted in STEM mode using X-ray energy dispersive spectrometry (XEDS). Precipitate sizes were measured using Adobe Photoshop, and number densities were determined based on the analyzed area and thickness measurements obtained via electron energy loss spectroscopy (EELS).

2.3 Microhardness (MH)

Microhardness was measured using a CM-802AT tester (Sun-Tec Corporation) with a 300 gf load and 12-second dwell time. 64 indentations were made across a 25 mm^2 area representative of the lower, middle, and upper regions of each sample. Data from unreliable indentations (due to soot and defects) in LPBF CrAZY3 were excluded.

3. Results

3.1 Phase analysis using XRD

Fig. 2 shows the powder XRD patterns and Rietveld refinement results for the FeCrAl samples, revealing the dominant α-Fe phase (body-centered cubic, Im-3m) in all LPBF-fabricated FeCrAl samples. While preferred orientations along (200) and (211) planes were present, Rietveld refinement demonstrated consistent lattice parameters (Table 2) across the samples, averaging ~2.887 Å – a slight expansion compared to pure α-Fe (2.8665 Å) [22] indicative of solid solution strengthening by alloying elements (Cr, Al, Zr, Y, O).

More significantly, Williamson-Hall analysis unveiled a strong correlation between LPBF processing conditions and the resulting α-Fe microstrain and crystallite size (Table 2). Specifically, LPBF CrAZY3, produced at a lower energy density, exhibited markedly elevated microstrain, signaling a high concentration of process-induced defects (analyzed further below). In contrast, LPBF CrAZY9, representing optimized LPBF parameters, displayed the lowest microstrain, indicative of a minimized defect density. LPBF CrAZY9 also exhibited the smallest crystallite size. These observations suggest that the interplay between crystallinity and defect concentration

dictates the α-Fe crystallite size within these LPBF-fabricated ODS alloys [23]. The absence of secondary phase peaks in micro-XRD point scans of LPBF CrAZY3's build surface, and the lack of peak shift, suggests that defect concentration is the cause in observed differences in hardness. The findings highlight the critical role of precise energy density control during LPBF to tailor the α-Fe microstructure and defect population, ultimately dictating the mechanical performance of these high-performance alloys.

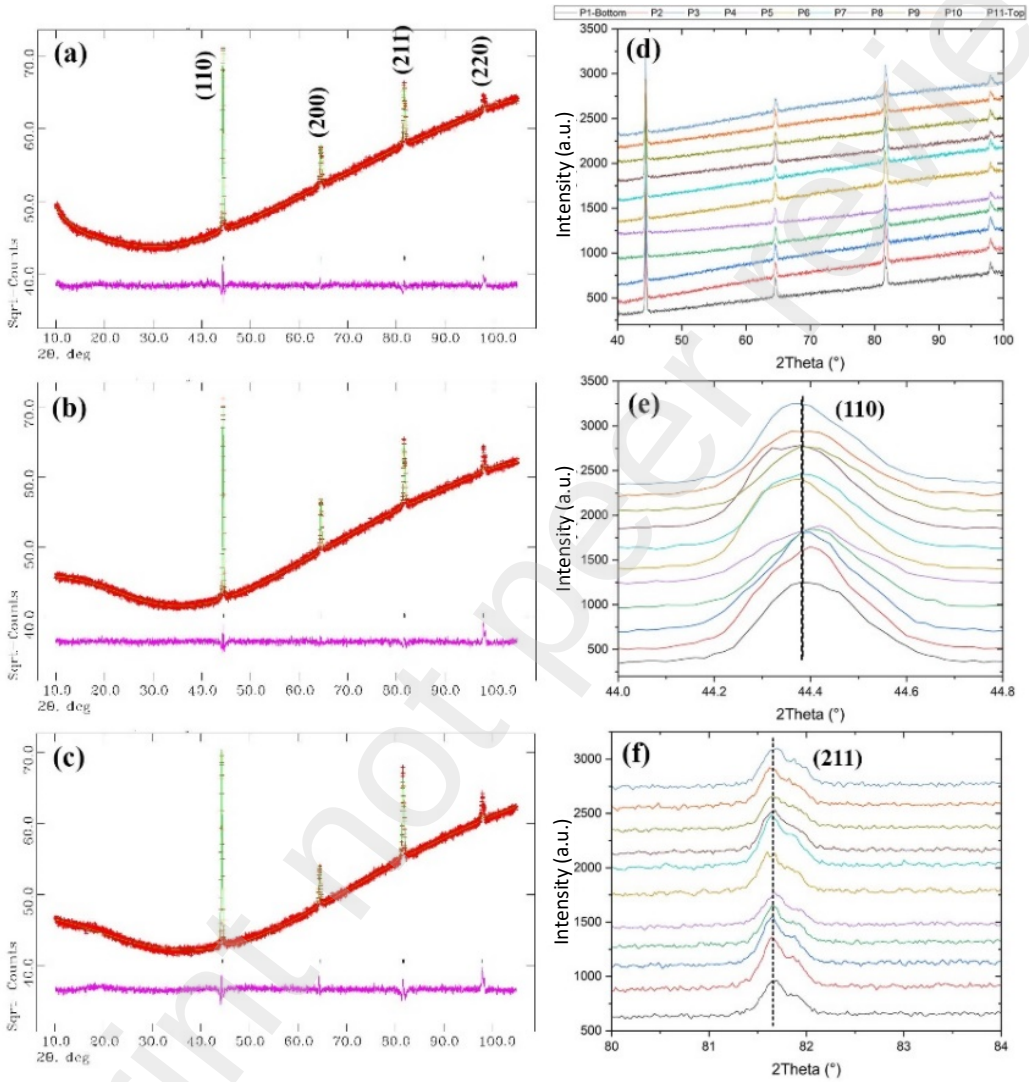

Fig. 1. (a-c) Experimental (red) and Rietveld-fitted (green) XRD patterns for LPBF CrAZY3, CrAZY9, and CrAZY12, respectively, with residuals (pink). Tick marks indicate the bcc Fe phase peak positions. (d-f) Micro-XRD point scans of the build direction surface for LPBF CrAZY3, showing the full XRD pattern (d) and magnified views of the (110) (e) and (211) (f) peaks.

Table 2. Summary of XRD results for the three LPBF-fabricated CrAZY samples, showing the Rietveld refinement goodness-of-fit (χ^2) values.

Sample #	L.P. (Å)	χ^2 of the fit	Crystallite size (nm)	μ-strain (%)	R^2 of W-H plot
CrAZY3	2.8868(1)	0.6	247	0.1080	99.8
CrAZY9	2.8874(1)	0.6	165	0.0756	99.7
CrAZY12	2.8872(1)	0.7	175	0.0901	99.9

3.2 Microstructural characteristics of Fe-Cr-Al-0.3Zr-0.3Y_2O_3 samples

Optical microscopy (Fig. 3) revealed stark differences in the microstructures of the three LPBF-fabricated Fe-Cr-Al-0.3Zr-0.3Y_2O_3 samples, directly correlating with the applied processing parameters. LPBF CrAZY3, fabricated at a lower energy density, exhibited a highly defective microstructure characterized by significant porosity and crack propagation originating from the sample edges (Fig. 3(a)). In contrast, LPBF CrAZY9 and, particularly, LPBF CrAZY12 displayed a substantially reduced pore density, with only isolated micro-sized pores visible. These observations underscore the critical sensitivity of LPBF-processed ODS alloys to energy density, where insufficient energy input (as in LPBF CrAZY3) results in incomplete melting and consolidation, leading to a highly porous and crack-prone microstructure. The correlation between processing conditions, defect density, and sample density directly highlights the need to be precise.

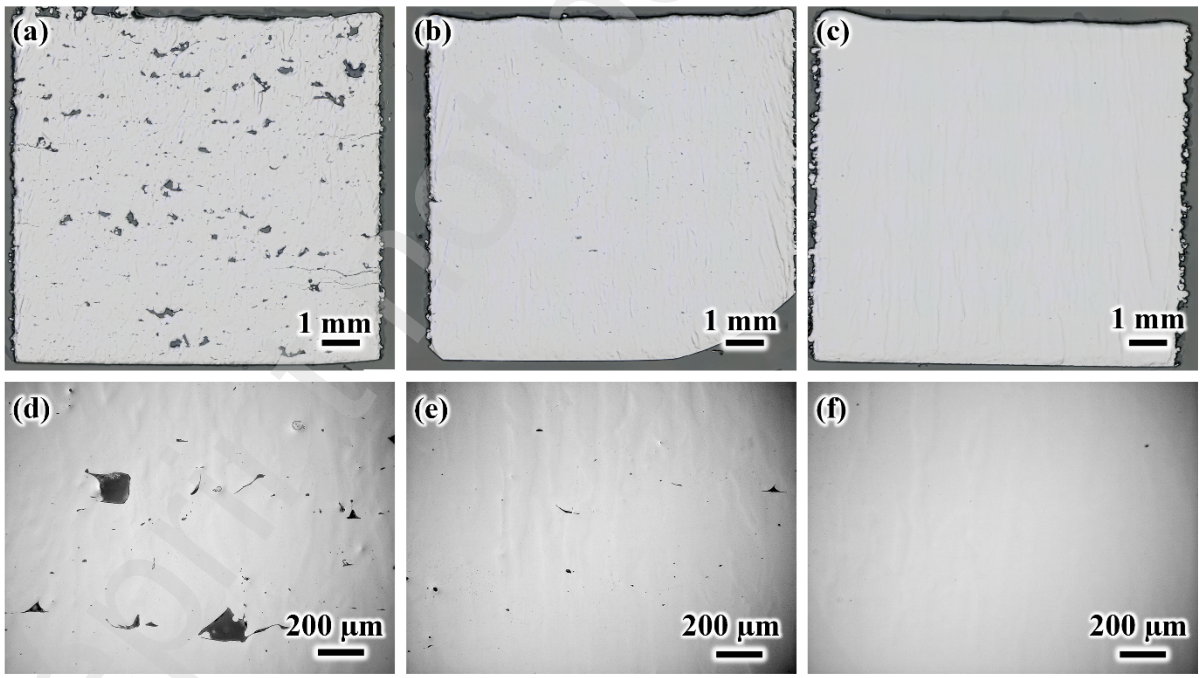

Fig. 3. (a–c) Low and (d–f) high magnification optical micrographs of LPBF CrAZY3 (a, d), CrAZY9 (b, e), and CrAZY12 (c, f). CrAZY3 clearly showed a significant lack of fusion, while CrAZY9 exhibited smaller lack of fusion pores, but still had a high density. Few pores were observed in the CrAZY12 samples, all being small, <25 μm^2 in area.

EBSD analysis revealed a highly textured microstructure in the LPBF CrAZY12 alloy, exhibiting a characteristic columnar grain morphology (Fig. 4(a-b)). Successful indexing of Kikuchi patterns, confirmed by matching with the body-centered cubic (BCC) structure (space group Im-3m) of α-Fe (ferrite), yielded a maximum band contrast of 205, indicating high pattern quality (Fig. 4(a)) and robust structure solution.

The columnar grains, aligned along the build direction, displayed a strong <100> crystallographic texture, a common feature in cubic systems [24]. This texture, visualized via Inverse Pole Figure (IPF) and Pole Figure (PF) maps (Fig. 4(b) and 4(c), respectively), reached a maximum multiples of uniform distribution (MUD) value of 13. This pronounced texture is attributed to epitaxial grain growth driven by the inherent thermal gradient and directional heat flux during LPBF [25, 26].

Further analysis of grain boundary misorientation angles revealed a significant fraction (70%) of high-angle grain boundaries (>10°), alongside a remaining 30% of sub-grain microstructures. Kernel Average Misorientation (KAM) mapping (Fig.4(d)) displayed predominantly low-to-moderate strain levels across the scanned area. The presence of moderate KAM angles (2.5°) in narrow grain regions suggests localized regions with slightly elevated strain levels within the sub-grain microstructure.

Finally, EBSD data indicated a mean grain size of 27.1 ± 12.2 µm, with grain sizes ranging from 17.8 to 153.8 µm. A summary of these microstructural parameters is presented in Table 3.

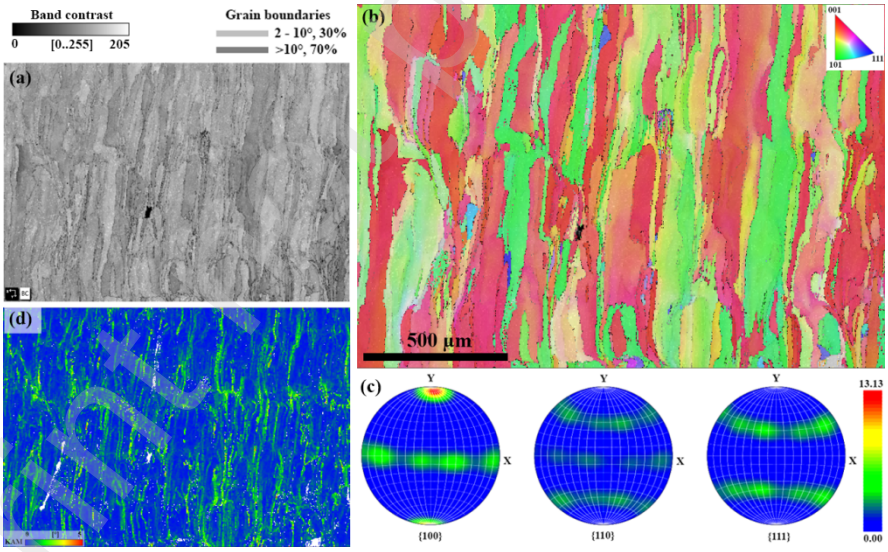

Fig. 2. EBSD data collected from the center of build direction surface of the LPBF CrAZY12. (a) Band contrast (BC) + grain boundary (GB) map, (b) BC + IPF + GB map, (c) PFs, and (d) KAM map.

EBSD analysis of LPBF CrAZY3 and LPBF CrAZY9 alloys revealed well-defined microstructures characterized by high band contrast (Table 3) and minimal unindexed areas (Fig. 5(a) and 5(c)). Similar to LPBF CrAZY12, both CrAZY3 and CrAZY9 exhibited a <100> crystallographic texture aligned parallel to the build direction. PF analysis yielded MUD values of 7.8 and 10.0 for CrAZY3

and CrAZY9, respectively, which were lower than the 13.0 MUD observed in CrAZY12. This indicates a progressively stronger <100> texture in the CrAZY series, with CrAZY12 exhibiting the most pronounced texture within the analyzed regions.
KAM mapping revealed minimal overall strain in the microstructures of both CrAZY3 (Fig. 5(e)) and CrAZY9 (Fig. 5(f)), with only localized regions of moderately elevated strain observed in sub-grain areas. Notably, average grain size also increased across the alloy series, with CrAZY12 exhibiting the largest grains compared to CrAZY3 and CrAZY9 (Table 3).

Remarkably, a clear trend emerged: both the <100> texture strength (MUD values) and average grain size increased systematically from LPBF CrAZY3 to CrAZY9 and further to CrAZY12. These findings strongly suggest that the texture development in these LPBF CrAZY alloys is driven by epitaxial grain growth along the build direction, directly proportional to the energy density employed during the LPBF process. Higher energy density appears to promote more pronounced epitaxial growth, resulting in larger grains and a stronger <100> texture.

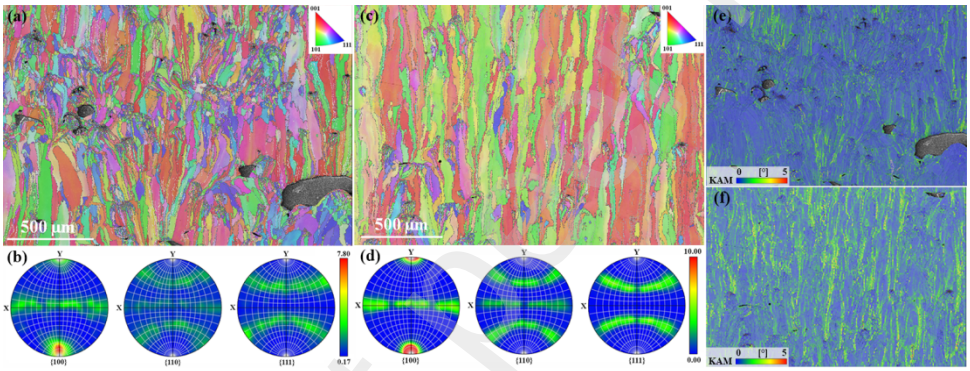

Fig. 3. BC + IPF + GB maps, PFs, and KAM maps of FeCrAl samples: (a, b, e) CrAZY3 and (c, d, f) CrAZY9.

Table 2. EBSD data of samples LPBF CrAZY3, LPBF CrAZY9, and LPBF CrAZY12.

Sample	**BC max.**	**Grain boundaries (%)**		**Max. MUD value of PFs**	**Grain size (µm)**		
		2 – 10°	>10°		Mean	Min.	Max.
LPBF CrAZY3	254	16.2	83.8	7.8	15.0±5.0	10.7	100.2
LPBF CrAZY9	255	35.9	64.1	10.0	20.4±7.1	14.3	77.3
LPBF CrAZY12	205	30	70	13.1	27.1±12.2	17.8	153.8

STEM analysis revealed the presence of secondary precipitates within the LPBF CrAZY12 alloy (Fig. 6(a)). Bright-field (BF) STEM imaging highlighted these precipitates as dark-contrast regions, while corresponding High-Angle Annular Dark-Field (HAADF) STEM images (Fig. 6(b)) displayed them in bright contrast, indicating the presence of high-Z (high atomic number) elements. High-resolution BF STEM images (Fig. 6(c) and 6(d)) corroborated the existence of these precipitates and further revealed a network of dislocations, including both line and loop-type configurations, along with nano-sized pore spaces.

Some circular-shaped large areas consist of pore character were present (Fig. 6(a) and 6(c), highlighted rectangles). These regions have possibly lost the precipitates during the FIB milling. High-resolution imaging revealed that some of the nano-sized pore spaces, previously identified at lower magnification, share similar characteristics (N1 in Fig. 6(c)). The elemental composition of these precipitates and pore-like regions was determined using X-ray Energy Dispersive Spectroscopy (XEDS) and is discussed in detail below.

Furthermore, observations revealed interactions between line dislocations and the identified nanoparticles/precipitates. These interactions suggest a potential influence of the secondary phase distribution on the mechanical properties of the LPBF CrAZY12 alloy, warranting further investigation.

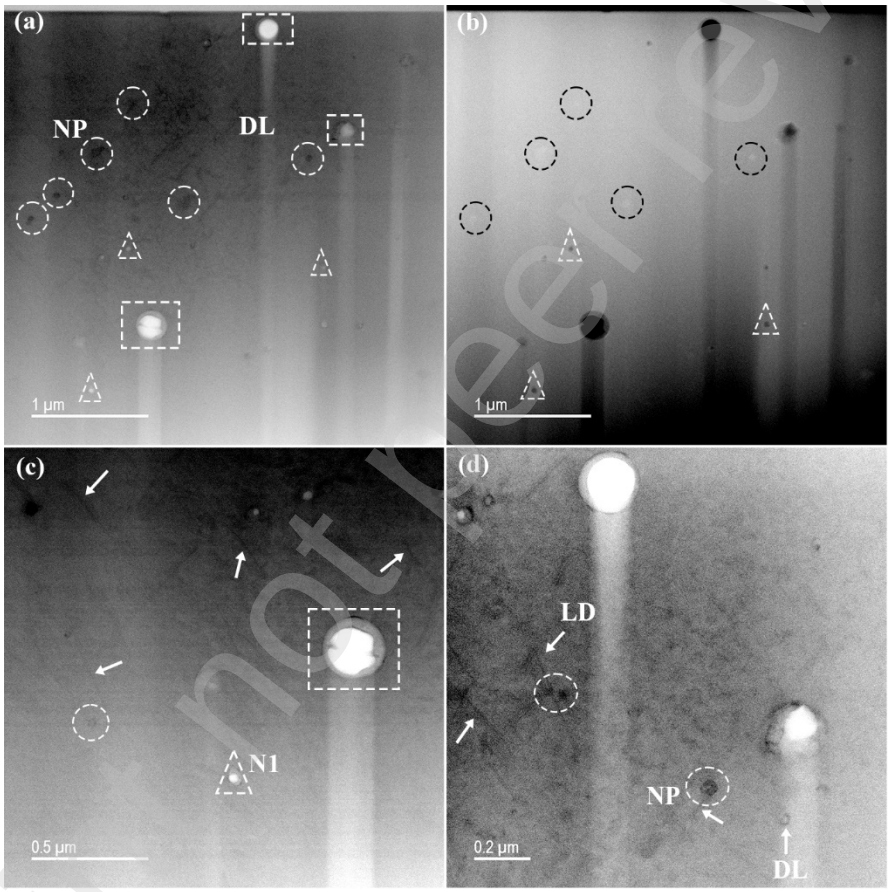

Fig. 4. STEM micrographs of LPBF CrAZY12: (a) Bright-field (BF) and (b) High-Angle Annular Dark-Field (HAADF) images. (c, d) High-resolution BF images. Nanoparticles (NP), pore spaces, and dislocations (LD: line dislocations, DL: dislocation loops) are indicated.

To determine the elemental composition of the observed precipitates, X-ray Energy Dispersive Spectroscopy (XEDS) mapping was performed on a representative area (inset, Fig. 7). The resulting elemental maps revealed that the precipitates are predominantly enriched in zirconium (Zr) and yttrium (Y). Furthermore, elevated concentrations of Zr, Y, and oxygen (O) were detected at the edges of some voids, suggesting potential oxide formation in these regions. While some Zr-rich particles exhibited minimal or no Y content, the overall distribution suggests that Y is also

present in solid solution within the CrAZY12 alloy matrix. Importantly, carbon (C) mapping at this resolution did not reveal any significant C enrichment within the analyzed region (data not shown).

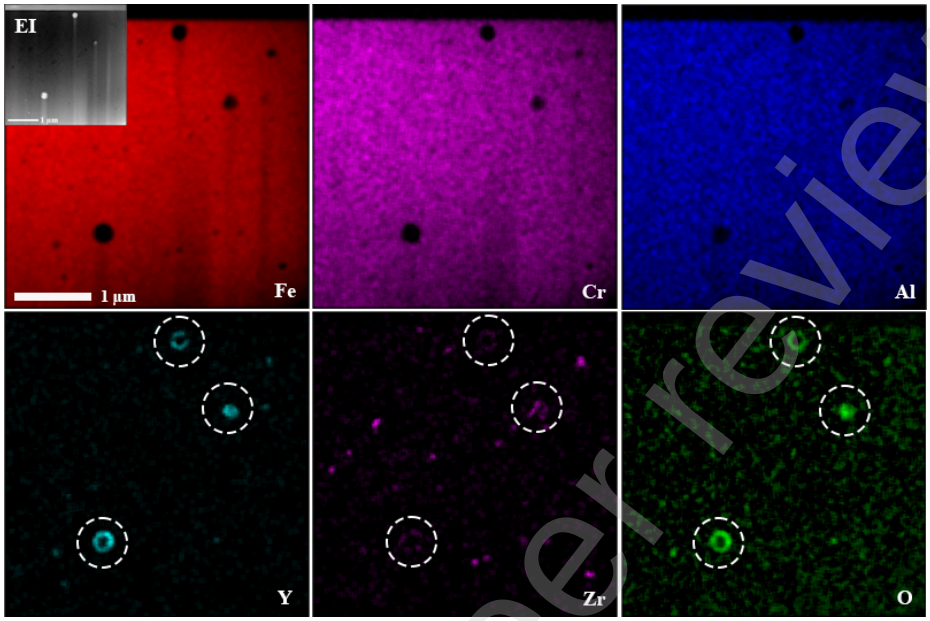

Fig. 5. XEDS elemental maps of an area of LPBF CrAZY12 sample. Inset on Fe map is the electron image (EI) of the sample area used. Some pore spaces with edges high in Y, Zr, and oxygen concentration are highlighted by circles.

High-resolution Scanning Transmission Electron Microscopy (STEM) further elucidated the microstructure of LPBF CrAZY12, revealing the co-existence of nanoparticles and line dislocations in another region of the sample (Fig. 8(a) and 8(b)). Notably, the presence of line dislocations and dark-contrast lines in proximity to a void area (VA in Fig. 8(a)) suggests the potential displacement of nanoparticles during Focused Ion Beam (FIB) milling. A representative nanoparticle (NP), exhibiting dark contrast in the Bright-Field (BF) STEM image (Fig. 8(a)) and corresponding bright contrast in the High-Angle Annular Dark-Field (HAADF) image (Fig. 8(b)), indicates enrichment with a high-Z element(s). X-ray Energy Dispersive Spectroscopy (XEDS) elemental mapping (Fig. 8(c)) confirmed that this nanoparticle is indeed rich in both zirconium (Zr) and yttrium (Y). Moreover, the slight carbon (C) enrichment coupled with oxygen (O) deficiency suggests that the nanoparticle is likely a Zr- and Y-rich carbide.

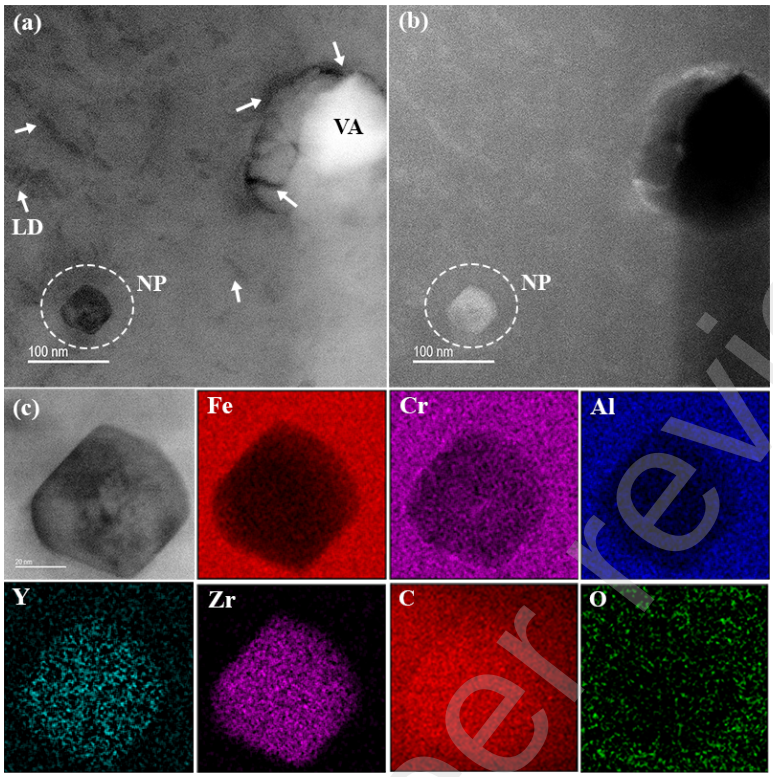

Fig. 6. (a) BF and (b) HAADF STEM images of another area of LPBF CrAZY12 sample at a higher resolution. (c) BF STEM image and the corresponding elemental maps of the nano precipitate highlighted in (a). LD, NP, and VA denote line dislocations, nanoparticles, and void areas, respectively.

Detailed TEM analysis revealed the microstructure surrounding FIB induced voids in LPBF CrAZY12 (Fig. 9(a)) to consist of a distinctive ring-like structure. This structure comprised an inner, bright-contrast ring and an outer, dark-contrast ring (Fig. 9(b)). Thicknesses varied, with the inner ring ranging from ~6 to 26 nm and the outer ring from ~13 to 30 nm. Notably, the inner ring contained ~2 nm nanoprecipitates (Fig. 9(c)). Elemental mapping (Fig.9(d-f)) identified the inner ring as Y- and O-rich, while the outer ring contained minor concentrations of Zr and C. These data strongly suggest the presence of Y_mO_n and Zr_xC_y type phases, with a Y-oxide dominating.

High-resolution TEM imaging (Fig. 9(c)) showed the Y- and O-rich inner ring to be composed of an amorphous matrix with embedded crystalline nanoparticles. Given the high Y and O concentrations, these nanoparticles are likely Y_2O_3, consistent with their established role in enhancing the mechanical strength of ODS steels [5].

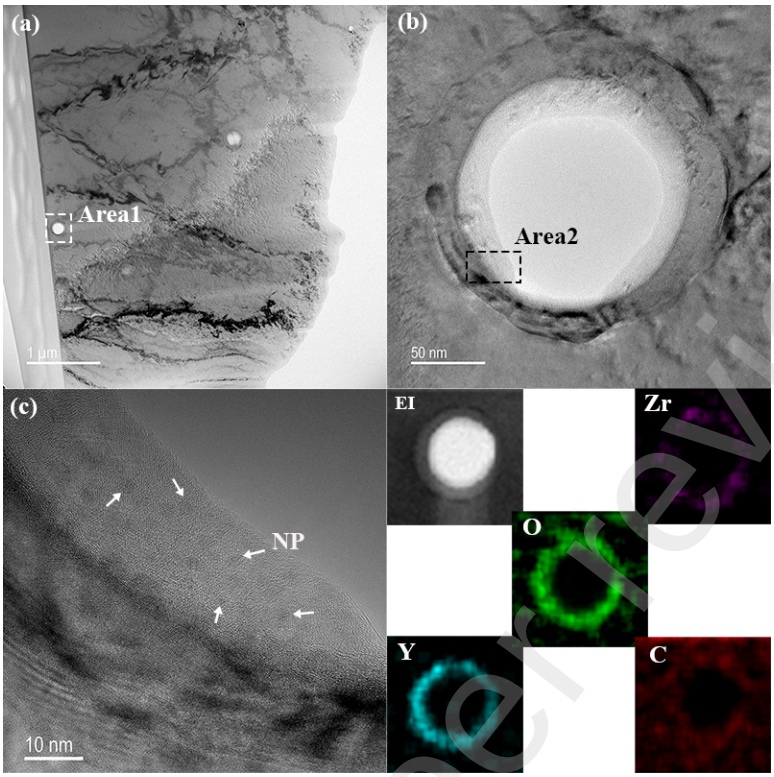

Fig. 7. BF TEM images of LPBF CrAZY12: (a) bulk sample, (b) a high-resolution BF TEM image of area 1 highlighted in (a), (c) a high-resolution BF TEM image of area 2 highlighted in (b), and the elemental maps of the void area in (b). Arrows highlight nanoprecipitates (NP) in (c). Al map is not shown since it did not show significant difference between the bulk material and ring areas.

While similar types of precipitates were observed in all three LPBF CrAZY samples, significant variations in precipitate size and distribution were evident. LPBF CrAZY3 (Fig. 10(a-b)) exhibited a noticeably higher density of finer precipitates compared to LPBF CrAZY9 (Fig. 10(d-e)) and LPBF CrAZY12 (Fig. 6 and 7). However, despite these microstructural differences, elemental maps suggested comparable overall concentrations of Zr- and Y-rich (oxide or carbide) particles across all three samples – a finding subsequently confirmed by quantitative precipitate number density measurements (Fig. 11). The presence of inner bright-contrast and outer dark-contrast ring structures surrounding particles, similar to those characterized in LPBF CrAZY12, was also observed in LPBF CrAZY3 and LPBF CrAZY9. Corresponding XEDS maps confirmed the enrichment of these rings in Zr and Y (Fig. 10(c,f)), providing further evidence for the presence of both oxide and carbide precipitates in all three LPBF CrAZY alloys.

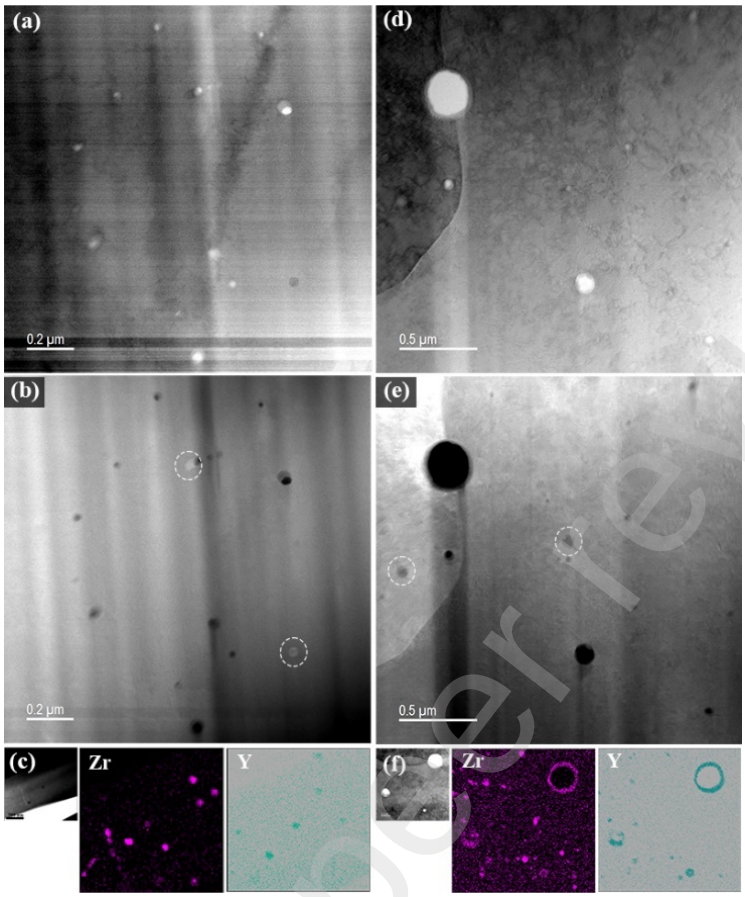

Fig. 8. Typical (a) BF and (b) HAADF STEM images of LPBF CrAZY3 sample. Typical (e) BF and (f) HAADF STEM images of LPBF CrAZY9 sample. Zr and Y elemental maps correspond to LPBF CrAZY3 and CrAZY9 sample areas depicted in (c) and (f), respectively are shown.

Quantitative TEM analysis (Fig. 11) revealed distinct nanoscale precipitate size distributions near the center of each LPBF CrAZY sample. LPBF CrAZY9 and LPBF CrAZY12 exhibited comparable distributions, with average precipitate diameters of 47 nm and 44 nm, respectively. In stark contrast, LPBF CrAZY3 displayed a significantly increased population of finer precipitates, resulting in a reduced average precipitate diameter of 38 nm. Despite these differences in size distribution, all three samples exhibited remarkably similar overall precipitate number densities, ranging from 6 to 8 × 10^{7} $cm^{-3.}$

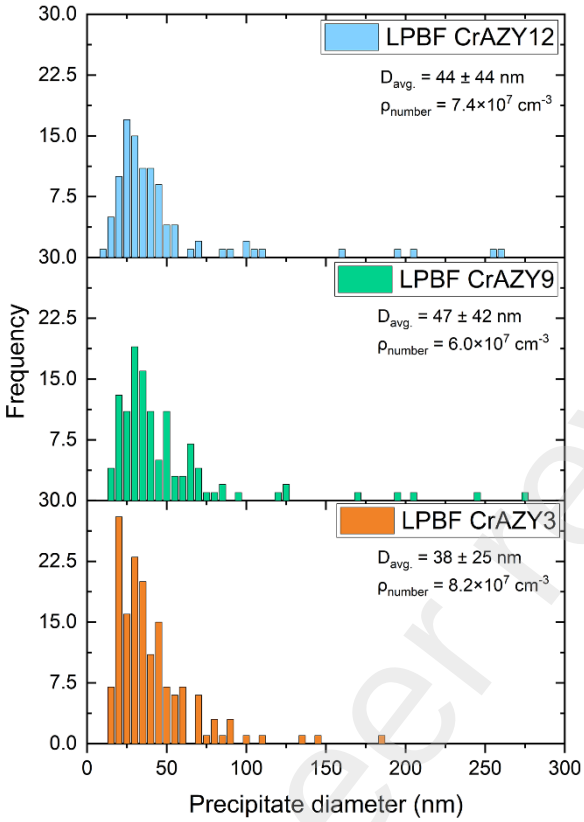

Fig. 9. Distributions of precipitate sizes of the samples.

3.3 Mechanical properties of LPBF CrAZY samples: Microhardness results

Microhardness measurements on LPBF CrAZY12 (Fig. 12) revealed a clear gradient along the build direction, with hardness increasing from top to bottom (200-250 HV, Table 4). While a similar trend was weakly observed in LPBF CrAZY3 and LPBF CrAZY9, their hardness distributions were more uniform. Notably, LPBF CrAZY12 exhibited the lowest average hardness, while LPBF CrAZY3 and LPBF CrAZY9 possessed the highest and nearly identical values. This inverse relationship between grain size and microhardness, particularly the lower hardness of the coarser-grained LPBF CrAZY12, aligns well with the Hall-Petch relationship [28, 29]. The microhardness values obtained in this study are also consistent with previously reported data for spark plasma sintered FeCrAl alloys [30], suggesting similar levels of mechanical strength can be achieved with LPBF.

Although there is a significant amount of literature on FeCrAl ODS alloys, there are no reported equations for predicting yield strengths based on Vickers hardness values. Therefore, the hardness and yield strength (YS) values for FeCrAl ODS were sourced from the literature [31, 32] and plotted in Fig. 12(b). The correlation between YS and hardness values is expressed by the equation H = 4.2084*YS - 6.6984, with a coefficient of determination (R^2) of 0.984. This equation was then used to predict YS values based on experimentally obtained Vickers hardness values in the current study. The corresponding values are listed in Table 4.

Table 3. Microhardness data of the CrAZY samples.

Sample	**Avg Hardness (HV)**	**Predicted YS (MPa)**
CrAZY3	261±11.1	609.8±27.5
CrAZY9	259.1±8	605.4±20.2
CrAZY12	226.4±9.5	529.2±23.7

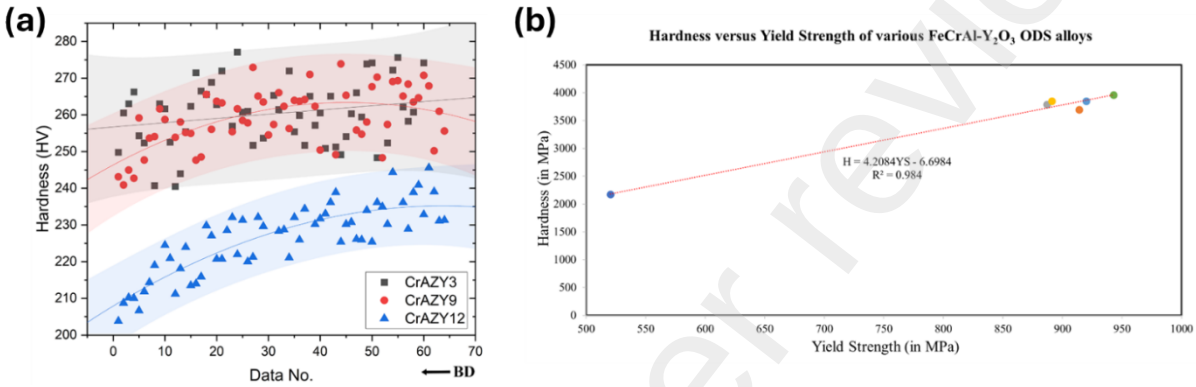

Fig. 10. (a) Vickers hardness distributions along the build direction (BD) for LPBF CrAZY samples, with 2nd-order polynomial fits and 95% prediction bands. And (b) Hardness versus Yield Strength of various FeCrAl-Y_2O_3 ODS alloys from literature [1, 2].

4. Discussion

4.1 Comparison of grain size and microhardness

Microstructural characterization via SEM/EBSD revealed a consistent, yet nuanced, response to LPBF processing in the Fe-Cr-Al-0.3Zr-0.3 Y_2O_3 alloys. All samples exhibited a columnar grain morphology, with grains elongated along the build direction and a preferential crystallographic texture parallel to α-ferrite planes. This texturing, a common characteristic of LPBF-fabricated materials, induces anisotropy. The intensity of this texture, quantified by the MUD value, varied with processing conditions; LPBF CrAZY12 exhibited the strongest texture, while the inadequate melting in LPBF CrAZY3, stemming from its lower energy density, hindered epitaxial grain growth and resulted in a weaker texture [33]. Kernel average misorientation (KAM) maps indicated minimal strain accumulation, except in regions with sub-grain structures, which are often observed within columnar grains in LPBF 304L and 316L stainless steels and have been linked to enhanced mechanical properties [30, 34].

Further SEM analysis revealed variations in precipitate distribution. In LPBF CrAZY12, fewer microscale (10 µm) precipitates were observed at the top surface compared to the center and bottom. However, smaller grain diameters were observed at the bottom of the build. Comparatively, LPBF CrAZY9 showed a more uniform precipitate distribution, but a generally smaller precipitate size than LPBF CrAZY12 (Fig. 13). Throughout LPBF CrAZY3, finer precipitates

were observed compared to both LPBF CrAZY9 and CrAZY12, and the low energy density resulted in a non-uniform structure characterized by inclusions, pores, and microcracks.

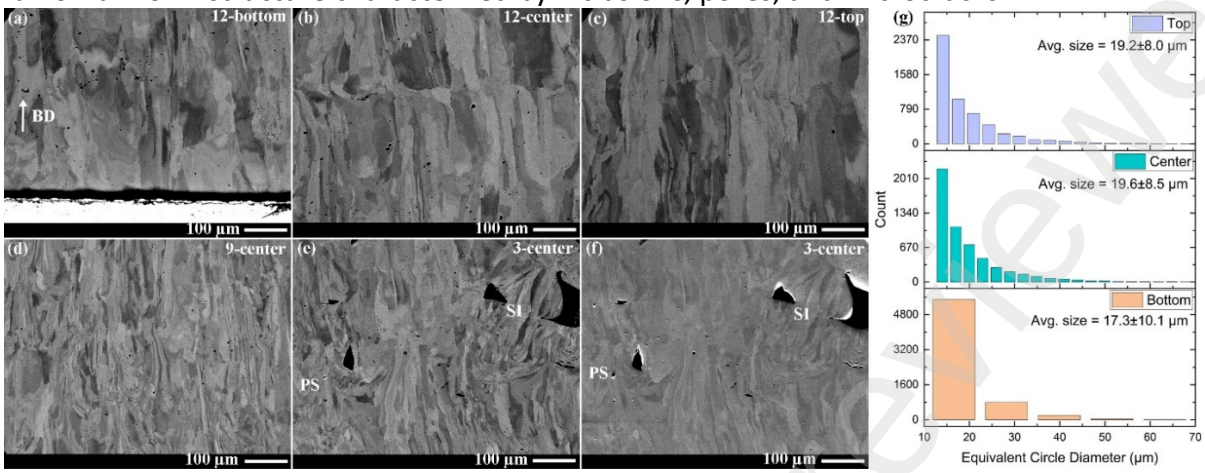

Fig. 11. BSE SEM images of LPBF CrAZY12 sample at the (a) lower, (b) center, and (c) upper parts of the build direction (BD). (d) BSE SEM images of LPBF CrAZY9 and (e) BSE and (f) SE SEM images of the center of LPBF CrAZY3. SI and PS denote soot inclusions and pore spacing, respectively. LPBF CrAZY12 shows a higher level of precipitates in the (a) bottom and (b) center areas than (c) top. (g) Grain size distribution of top, center, and bottom areas of LPBF CrAZY12 sample.

XEDS elemental mapping identified nano- to micro-sized precipitates of MOx and MCx type (where M = Y and/or Zr) in all LPBF CrAZY samples. However, some Zr-rich particles exhibited depleted Y levels, indicating Y dissolution within the α-Fe matrix during LPBF processing. This, in addition to already being low in number of precipitates, made studying uniformity difficult. While mechanically alloyed ODS Fe-Cr-Al alloys with similar compositions typically exhibit both Zr carbides and Y-Al oxides [19], the precipitates in these LPBF-fabricated samples showed limited Al content, suggesting the 0.3 wt.% Zr and 0.3 wt.% Y_2O_3 additions inhibit Al segregation from the Fe-Cr-Al solid solution. This would promote higher strength of ODS alloys because it inhibits the Cr rich alpha prime.

Microhardness measurements revealed a clear trend; LPBF CrAZY12 exhibited the lowest average hardness (204 – 246 HV), LPBF CrAZY9 had intermediate values (241 – 274 HV), and LPBF CrAZY3 displayed the highest hardness (230 – 288 HV). The grain size distributions correlated inversely with these hardness values; LPBF CrAZY3 had the largest portion of finer grains, while the grain size distribution shifted towards larger sizes from LPBF CrAZY3 to LPBF CrAZY9 and LPBF CrAZY12 (Fig. 14). The result shows an inverse relationship with the hardness. This suggests that Hall-Petch relationship dominates.

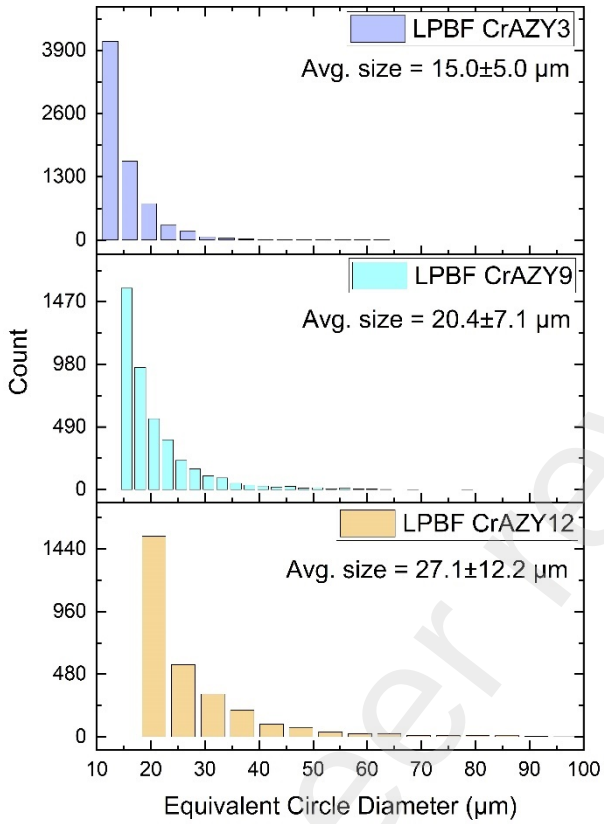

Fig. 12. The distribution of equivalent circle diameter of grains of LPBF CrAZY samples.

4.2 Estimated Sink Strength

A critical finding was the low precipitate number density (6 – 8×107 cm-3) measured in all LPBF CrAZY samples, significantly lower than the 10^23 m^{-3} expected for high-performance ODS FeCrAl alloys [14, 24]. This translates to a low calculated precipitate sink strength (~2.0×10^7 m-2), far below the ~10^15 m^{-2} deemed necessary for radiation resistance in advanced fission reactors operating at high temperatures (T/TM ratio of 0.3 – 0.6. The sink strength was calculated based on the formula reported by Massey et al. [18]:
$S_p = 4\pi R_P N_P$, where S_p is the precipitate sink strength, while Rp and Np are precipitate radius and number density, respectively.

Such a low sink strength enhances the radiation-induced formation of α'-phase precipitates and Cr segregation, as observed in ODS 14YWT alloys [35]. Although radiation induced elemental segregation was only a small amount, these changes significantly influence ODS 14YWT mechanical properties [4]. These findings strongly suggest that post-processing heat treatments are crucial for inducing Y-rich secondary precipitate nucleation in LPBF CrAZY samples [5, 6]. Further investigations must focus on optimizing LPBF processing parameters to achieve high enough precipitate density and a desirable sink strength in ODS FeCrAl alloys designed for extreme irradiation environments.

5. Conclusions

Integrated microstructural and mechanical characterization revealed key insights into the LPBF-fabricated Fe-Cr-Al-0.3Zr-0.3Y_2O_3 alloys, highlighting the complex interplay between processing parameters, microstructure, and properties.

- Macroscopic XRD confirmed a single α-ferrite phase in all LPBF-fabricated Fe-Cr-Al-0.3Zr-0.3Y_2O_3 samples, with no significant crystallographic variations across the build direction.
- TEM/STEM revealed the presence of nano- to micro-sized Y-, Zr-, O-, and C-rich precipitates (MOx, MCy phases), as anticipated for ODS alloys.
- LPBF CrAZY3 exhibited significant microcracking and porosity due to low energy density processing, contrasting with the minor porosity in LPBF CrAZY9 and LPBF CrAZY12, correlating with density measurements.
- SEM/EBSD showed columnar grains oriented along the build direction, with a [4] texture exhibiting highest and minimum textures in LPBF CrAZY12 and LPBF CrAZY3, respectively.
- EBSD revealed that LPBF CrAZY12 had the highest mean grain size, while LPBF CrAZY3 had the lowest. The samples were shown to be relatively residual stress free
- Results correlated well with prior Hall-Petch studies with results such as LPBF CrAZY12 had the lowest value while LPBF CrAZY3 having the highest.
- Secondary precipitate densities (10^7 cm^{-3}) and corresponding sink strengths (10^7 m^{-2}) were significantly lower than desired for effective ODS behavior and radiation resistance. The low result is a great need for future study.

Therefore, further process optimization and tailored post-processing of the LPBF AM fabricated Fe-Cr-Al-0.3Zr-0.3Y_2O_3 is to be tested with further experimentations focusing on LPBF conditions in acquiring desirable precipitate densities and mechanical properties of ODS FeCrAl.

CRediT authorship contribution statement

Subhashish Meher: Conceptualization, data curation, formal analysis, investigation, methodology, validation, writing –original draft. **Chinthaka M. Silva:** Conceptualization, data curation, formal analysis, investigation, methodology, validation. **Holden Hyer:** Conceptualization, data curation, formal analysis, investigation, methodology, validation, writing – review and editing. **Tanvi A. Ajantiwalay:** Data curation, formal analysis, investigation, methodology, validation, writing – review and editing. **Shalini Tripathi:** Conceptualization, data curation, formal analysis, investigation, methodology, validation. **Angel Ortiz:** Data curation, methodology. **Quin R. S. Miller:** Data curation, methodology, writing – review and editing. **Nathan Canfield:** Data curation, methodology. **Mohan Sai Kiran Kumar Yadav Nartu:** Data curation, methodology, writing – review and editing. **Sebastien Dryepondt:** Conceptualization, data curation, formal analysis, investigation, methodology, validation, writing – review and editing. **Isabella J. van Rooyen:** Conceptualization, funding acquisition, investigation,

methodology, project administration, resources, supervision, validation, writing – review and editing.

Data Availability

Data will be made available on request from the corresponding authors.

Declaration of Competing Interest

The authors declare that they have no known competing financial interests or personal relationships that could have appeared to influence the work reported in this paper.

Acknowledgments

The research presented here was supported by the Advanced Materials and Manufacturing Technology (AMMT) program of the U.S. Department of Energy (DOE) Office of Nuclear Energy. PNNL is a multi-program national laboratory operated for the DOE by Battelle Memorial Institute under Contract No. DE-AC05-76RL01830.

References

[1] S. Ukai, M. Fujiwara, Perspective of ODS alloys application in nuclear environments, Journal of Nuclear Materials 307-311 (2002) 749-757.
[2] B.N. Goshchitskii, V.V. Sagaradze, V.I. Shalaev, V.L. Arbuzov, Y. Tian, W. Qun, S. Jiguang, Structure, radiation resistance and thermal creep of ODS ferritic steels, Journal of Nuclear Materials 307-311 (2002) 783-787.
[3] B.A. Pint, I.G. Wright, Long-term high temperature oxidation behavior of ODS ferritics, Journal of Nuclear Materials 307–311 (2002) 763–768.
[4] M.A. Auger, D.T. Hoelzer, K.G. Field, M.P. Moody, Nanoscale analysis of ion irradiated ODS 14YWT ferritic alloy, Journal of Nuclear Materials 528 (2020) 151852.
[5] T. Boegelein, S.N. Dryepondt, A. Pandey, K. Dawson, G.J. Tatlock, Mechanical response and deformation mechanism of ferritic oxide dispersion strengthen steel structures produced by selective laser melting, Acta Materialia 87 (2015) 201–215.
[6] T. Boegelein, E. Louvis, K. Dawson, G.J. Tatlock, A.R. Jones, Characterization of a complex thin walled structure fabricated by selective laser melting using a ferritic oxide dispersion strengthened steel, Materials Characterization 112 (2016) 30–40.
[7] S.J. Zinkle, G.S. Was, Materials challenges in nuclear energy, Acta Materialia 61(3) (2013) 735-758.
[8] C.P. Massey, K.A. Terrani, S.N. Dryepondt, B.A. Pint, Cladding burst behavior of Fe-based alloy under LOCA, Journal of Nuclear Materials 470 (2016) 128–138.
[9] K.G. Field, X. Hu, K.C. Littrell, Y. Yamamoto, L.L. Snead, Radiation tolerance of neutron-irradiated model Fe-Cr-Al alloys, J. Nucl. Mater. 465 (2015) 746–755.

[10] C. Capdevila, M.K. Miller, I. Toda, J. Chao, Influence of the α–α′ phase separation on the tensile properties of Fe-base ODS PM2000 alloy, Mater Sci Eng 527 (2010) 7931–7938.
[11] S.A. Briggs, P.D. Edmondson, K.C. Littrell, Y. Yamamoto, R.H. Howard, C.R. Daily, K.A. Terrani, K. Sridharan, K.G. Field, A combined APT and SANS investigation of α′ phase precipitation in neutron-irradiated model FeCrAl alloys, Acta Mater 129 (2017) 217–228.
[12] P.D. Edmondson, S.A. Briggs, Y. Tamamoto, R.H. Howard, K. Sridharan, K.A. Terrani, K.G. Field, Irradiation-enhanced α′ precipitation in model FeCrAl alloys, Scripta Materialia 116 (2016) 112–116.
[13] S. Dryepondt, K.A. Unocic, D.T. Hoelzer, C.P. Massey, B.A. Pint, Development of low-Cr ODS FeCrAl alloys for accident-tolerant fuel cladding, J Nucl Mater 501 (2018) 59–71.
[14] L. Marechal, B. Lesage, A.M. Huntz, R. Molins, Oxidation behavior of ODS Fe-Cr-Al alloys: Aluminum depletion and lifetime, Oxid Met 60 (2003) 1–28.
[15] G. Chen, H. Yang, H. Sun, F. Wang, H. Wang, Q. Kong, X. An, Y. Zhang, J. Wang, Exploring the high-temperature steam oxidation behavior of the lean-Cr (7–10 wt.%) FeCrAl alloys, Corrosion Science 194 (2022) 109927.
[16] M.E. Alam, S. Pal, K. Fields, S.A. Maloy, D.T. Hoelzer, G.R. Odette, Tensile deformation and fracture properties of a 14YWT nanostructured ferritic alloy, Materials Science & Engineering A 675 (2016) 437–448.
[17] J.H. Kim, T.S. Byun, D.T. Hoelzer, Tensile fracture characteristics of nanostructured ferritic alloy 14YWT, Journal of Nuclear Materials 407 (2010) 143–150.
[18] C.P. Massey, S.N. Dryepondt, P.D. Edmondson, M.G. Frith, K.C. Littrell, A. Kini, B. Gault, K.A. Terrani, S.J. Zinkle, Multiscale investigations of nanoprecipitate nucleation, growth, and coarsening in annealed low-Cr oxide dispersion strengthened FeCrAl powder, Acta Materialia 166 (2019) 1–17.
[19] C.P. Massey, P.D. Edmondson, K.A. Unocic, Y. Yang, S.N. Dryepondt, A. Kini, B. Gault, K.A. Terrani, S.J. Zinkle, The effect of Zr on precipitation in oxide dispersion strengthened FeCrAl alloys, Journal of Nuclear Materials 533 (2020) 152105.
[20] A.C. Larson, R.B. Von Dreele, General Structure Analysis System (GSAS), Los Alamos National Laboratory, 2000.
[21] C.M. Silva, B.C. Childs, M.G. Ferrier, M.M. Greenough, K.S. Holliday, Phase stability of uranium monocarbide under laser irradiation in argon and methane environments, Journal of Nuclear Materials 509 (2024) 154839.
[22] E.A. Owen, E.L. Yates, Precision measurements of crystal parameters, Philosophical Magazine (1933) 472–488.
[23] R. Jenkins, R.L. Snyder, Introduction to X-ray Powder Diffractometry, John Wiley & Sons, Inc.1996.
[24] M. Ghayoor, K. Lee, Y. He, C.H. Chang, B.K. Paul, Selective laser melting of 304L stainless steel: role of volumetric energy density on the microstructure, texture and mechanical properties, Additive Manufacturing 32 (2020) Article number: 101011.
[25] K. Hagihara, T. Nakano, Control of anisotropic crystallographic texture in powder bed fusion additive manufacturing of metals and ceramics, JOM 74 (2022) 1760–1773.
[26] Y. Wang, B. Wang, L. Luo, B. Li, B. Su, D. Chen, T. Liu, L. Wang, Y. Su, J. Guo, H. Fu, Build atmosphere aided texture control in additively manufactured FeCrAl steel by laser powder bed fusion, Scripta Materialia 239 (2024) Article number: 115806.

[27] P.K. Parida, A. Dasgupta, V. Srihari, C. Ghosh, R. Basu, R. Mythili, S. Dhara, Structural investigations of Y2O3 dispersoids during mechanical milling and high-temperature annealing of Fe-15Y2O3-xTi (x= 0–15) model ODS alloys, Advanced Powder Technology 31 (2020) 1665–1673.
[28] E.O. Hall, The deformation and ageing of mild steel: III discussion of results, Proc Phys Soc Sect B 64(9) (1951) 747–755.
[29] N.J. Petch, The cleavage strength of polycrystals, J Iron Steel Inst 174(1) (1953) 25–28.
[30] R. Ding, H. Wang, Y. Jiang, R. Liu, K. Jing, M. Sun, R. Zhang, S. Qiu, Z. Xie, H. Deng, X. Wang, M. Kong, W. Jiang, Q. Fang, C. Liu, Effects of ZrC addition on the microstructure and mechanical properties of Fe-Cr-Al alloys fabricated by spark plasma sintering, Journal of Alloys and Compounds 805 (2019) 1025–1033.
[31] H. Jia, R. Zhang, D. Long, Y. Sun, Z. Zhou, Effect of zirconium content on mechanical properties of ODS FeCrAl alloy, Materials Science and Engineering: A 839 (2022/04/06).
[32] B.C. Maji, S. Ukai, N. Oono-Hori, Microstructural stability and intermetallic embrittlement in high Al containing FeCrAl-ODS alloys, Materials Science and Engineering: A 807 (2021/03/11).
[33] A. Li, Q. Chen, P. Wang, J. Mao, X. Wu, H. Xin, Z. Fang, C. Teng, L. Wu, J. Tang, Laser powder bed fusion of oxide dispersion strengthened FeCrAl alloy: Processing and microstructural evolution, Material Characterization 208 (2024) Article number: 113590.
[34] R.S. Thanumoorthy, J.K. Chaurasia, V.A. Kumar, P.I. Pradeep, A.S.S. Balan, B. Rajasekaran, A. Sahu, S. Bontha, Effect of build direction on anisotropy in tensile behavior of laser powder bed fusion fabricated SS316L, Journal of Material Engineering and Performance (2023).
[35] E. Aydogan, E. Martinez, K. March, O. El-Atwani, D.L. Krumwiede, P. Hosemann, T. Saleh, S.A. Maloy, α' formation kinetics and radiation induced segregation in neutron irradiated 14YWT nanostructured ferritic alloys, Scientific Reports 9 (2019) 8345.